Journal of Casting & Materials Engineering Vol. 9 No. 1 (2025) 1–7
https://doi.org/10.7494/jcme.2025.9.1.1

3D Microstructure Reconstruction of Tetragonal Zirconia Polycrystalline

Grzegorz Grabowski

AGH University of Krakow, Faculty of Materials Science and Ceramics, 30 Mickiewicza Av., 30-059 Krakow, Poland
e-mail: grzegorz.grabowski@agh.edu.pl

Received: 13 February 2025/Accepted:10 March 2025/Published online: 28 March 2025.
This article is published with open access at AGH University of Science and Technology Journals.

Abstract

The microstructure of a material is fundamental to its properties and behavior under mechanical and thermal loads. Understanding the internal structure of a material and controlling the microstructure at the stage of ceramic materials synthesis are essential for designing materials with desired properties. This study focuses on the three-dimensional reconstruction of the microstructure of yttria-stabilized tetragonal zirconia polycrystalline (TZP). The goal was to create accurate digital models of the microstructure which could be used for further material analysis.

The study utilized images obtained through scanning electron microscopy (SEM), on the basis of which the fundamental stereological parameters were determined. The microstructure reconstruction was performed using the Laguerre tessellation method, allowing for the generation of three-dimensional digital models of the microstructure that represent the material's internal structure.

The results confirm that, based on the basic stereological parameters obtained from two-dimensional cross-sections, three-dimensional reconstruction of the microstructure of polycrystalline zirconia is possible. This work, therefore, represents a step towards the effective design of ceramic materials with high performance parameters, through the control and optimization of their microstructure.

Keywords:

microstructure, polycrystals, tessellation, 3D reconstruction, simulations

1. INTRODUCTION

Microstructure has a fundamental impact on the properties of polycrystalline ceramic materials. The grain size, shape and orientation significantly influence, and sometimes even determine, many of the material's key properties on a macro-scale [1]. Therefore, analyzing the interactions between individual grains is essential for a complete description of the deformation mechanism occurring under mechanical and thermal loads. Additionally, the grain boundaries, which are disturbances in the ideal crystalline structure, determine many transport phenomena, such as heat transfer or electric current flow, but also have a significant impact on fracture or high-temperature plasticity mechanisms. Understanding these phenomena occurring at the level of individual grains, and controlling the microstructure at the synthesis stage, are therefore essential for the effective design of ceramic materials with desired mechanical, thermal, and electrical properties.

Research into the interactions between grains and their influence on the macroscopic behavior of materials constitutes a key area for achieving progress in the field of materials engineering. However, for such research to be possible, an increasingly accurate description of the microstructural structure of a material is required. For this purpose, alongside measurement methods, techniques for generating three-dimensional digital models of microstructure are being developed. These models, providing a virtual equivalent of real polycrystalline materials, are used for both extended microstructure analysis (3D) and in numerical simulations, which are aimed at investigating the macroscopic properties of materials. Digital models of microstructure thus form the basis for *in-silico* research, which complement and extend experimental methods, allowing for a better understanding of the phenomena being analyzed and reducing the costs of both basic and applied research.

Methods used for reconstructing microstructure in the form of digital material models can be divided into two main kinds. One are reconstructions based directly on experimental data, obtained by X-ray tomography techniques (X-ray microtomography) [2–6], scanning microscopy or backscattered electron diffraction combined with FIB technique, using a focused ion beam (SEM/FIB, EBSD/FIB) [7–10]. The techniques in this stream, combined with advanced algorithms for data acquisition and analysis, allow for the reproduction of three-dimensional microstructure in the form of

digital models [11]. In recent years, these techniques have developed rapidly, however, they are still not widely used due to technical issues related to, among others, the long data acquisition time, limited size of the analyzed space, and equipment costs [12].

The second direction of microstructure reconstruction is associated with simulation methods, where experimental data is used in a limited scope, and sometimes only at the stage of verifying the obtained results [13, 14]. Commonly used methods in this stream include: the Monte Carlo method (Monte Carlo Potts) [15, 16], cellular automata [17–19], and tessellation used in this work [20–23]. Such reconstructive approaches enable the attainment of microstructure models that are statistically equivalent to models fully based on experimental data [24], but also allow for simulations of virtual microstructure variability over time. This facilitates, for example, the analysis of grain growth during sintering [25, 26]. The rapid development of algorithms, combined with the increasing computational power of workstations, enables the generation of synthetic microstructures that can serve as a basis for further numerical analyses conducted, for example, with the Finite Element Analysis (FEA) method [1, 21, 22, 27].

2. MATERIAL AND METHODS

Microstructure reconstruction was conducted for yttria-stabilized polycrystalline zirconia (TZP). The material for the study was obtained from commercial 3Y-TZP powder (TOSOH), sintered freely at 1400°C. Samples obtained in this way were polished, and their surface was additionally etched thermally at 1300°C for 0.5 h. Imaging was performed using the SEM technique with a Nova NanoSEM 200 – FEI microscope in low vacuum mode using a high-resolution Helix detector. An example image of the microstructure of the analyzed polycrystalline zirconia is shown in Figure 1a.

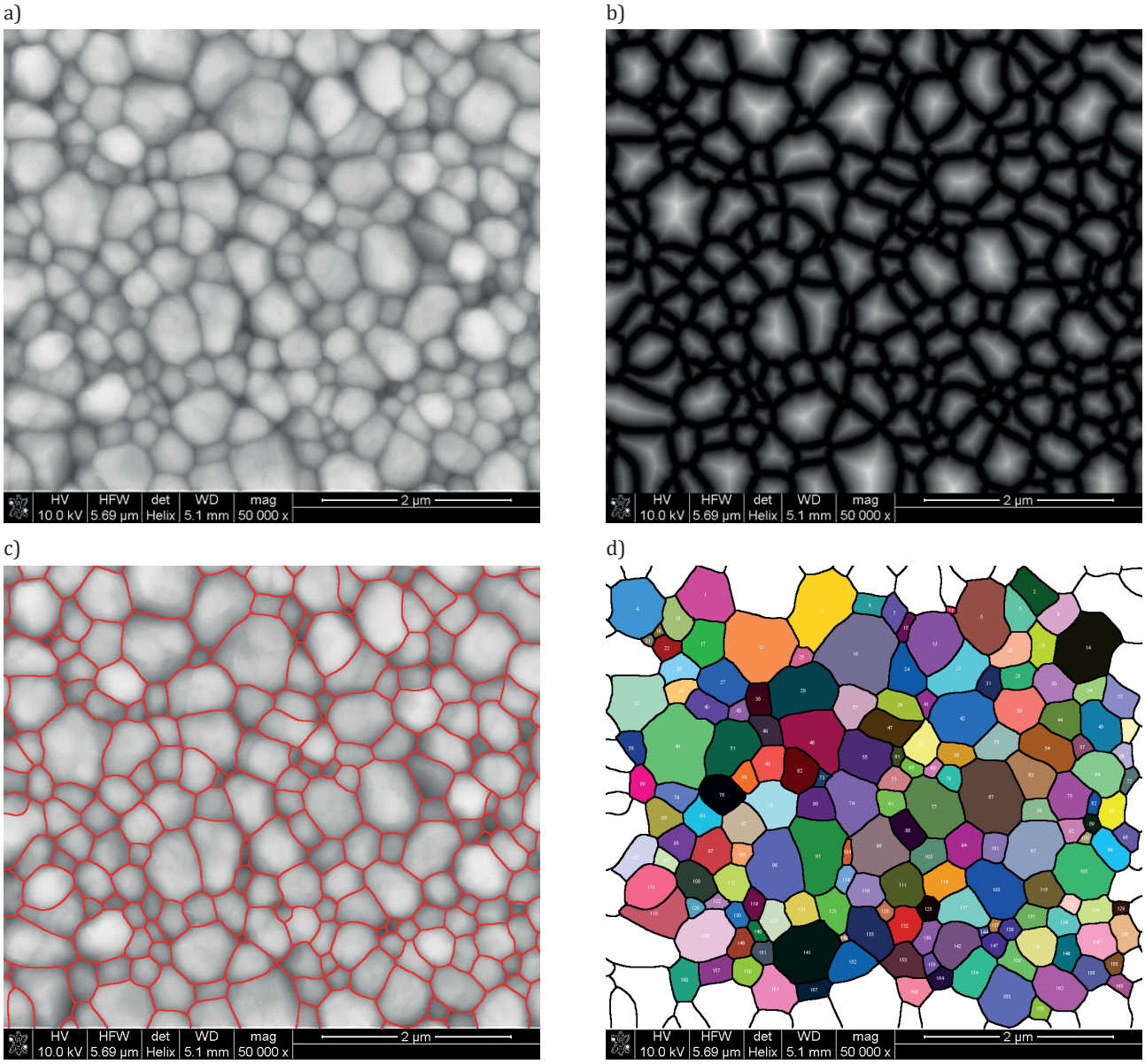

Fig. 1. The main stages of processing and analyzing images of the TZP: (a) SEM source image; (b) Euclidian Distance Map; (c) SEM image with overlay binary image (red); (d) image after segmentation and indexation prepared for quantitative analysis (colors used only to mark consecutive grains; particles lying on the edge of the image not included in the analysis, marked in white)

The acquired microstructure images were then subjected to processing operations to obtain binary images, which were finally analyzed. Image processing began with typical operations, including noise removal (median filter), contrast and brightness leveling (histogram adjustment). Subsequently, a background alignment operation was performed using the rolling ball algorithm [28]. The images prepared in this way were subjected to binarization. To emphasize the positions of the grain boundaries, the binary images were transformed into a Euclidean Distance Map [29], and based on these, Morphological Segmentation was performed [30], which led to the reconstruction of the grain boundaries. The entire image processing work was conducted using the *ImageJ* software (Public Domain license) [31] and, for automation, recorded in the scripts. Through this approach, utilizing batch processing of the entire series of SEM images, all binary images were obtained with identical parameters and processing steps. Finally, the binary images of the microstructure, obtained in the processing process, were subjected to manual correction, involving the removal of artifacts from the image and sometimes local modification of some boundary courses. The prepared binary images were segmented and indexed, and then basic stereological parameters were determined for the obtained particles: particles area A, particles perimeter L, particles number N, and Feret diameters: maximum $d^F_{\max}$ and minimum $d^F_{\min}$, angle for the maximum Feret diameter $\theta_{\max}$. Based on the determined parameters, the equivalent diameter $d_{\mathrm{eq}} = 2\sqrt{A/\pi}$ and the circularity shape descriptor $f_c = 4\pi A/^{\mathrm{L2}}$, solidity shape descriptor $f_s = \pi d^2_{\mathrm{eq}}/(4\mathrm{A})$ were also calculated.

To obtain information about the diameter distribution for the three-dimensional grains of the analyzed polycrystals, the Scheil–Schwartz–Saltykov (SSS) method was applied [32–34]. For this purpose, the equivalent diameter values of the indexed particles were divided into 15 classes (k = 15) with width Δ, and histograms were created showing the number of particles (2D) per unit area N_A in subsequent diameter intervals d_i (i = 1, …, k). Using the Saltykov correction factor a_{ij}, which was generally presented by Takahashi and Suito [35], the number of grains (3D) per unit volume N_V, contained in subsequent (k) classes, was calculated:

$$N_V(j) = \frac{1}{\Delta}\sum_{i=j}^{k} a_{ij} N_A(i) \tag{1}$$

The diameter distribution of equivalent grains (3D) obtained in this way was used for the reconstruction of the microstructure.

The reconstruction of the microstructure of polycrystalline zirconia was conducted using the Laguerre tessellation method. This method is known as a weighted Voronoi tessellation and is based on dividing the space Ω into cells (grains), whose area C_i is given by the expression [1]:

$$C_i = \{x \in \Omega: \|x - S_i\|^2 - w_i < \|x - S_j\|^2 - w_j\}, \text{ for } j \neq i \tag{2}$$

where $\|x - S_i\|$ is the distance (Euclidean metric) between any point x belonging to the analyzed space Ω and a chosen seed point S_i, while S_j is the seed point of another cell C_j from this space. In Laguerre tessellation, the distance of point x from the seed point S_i is additionally modified by a weight coefficient w_i, which can be interpreted as a parameter defining the radius of a sphere r_i (or a circle in 2D), whose center is located at the seed point S_i ($r_i = \sqrt{w_i}$). In practice, assigning a specific weight to each seed point enables the adjustment of the cell size distribution in the generated structure to a hypothetical or empirical distribution of crystallite sizes, allowing for a closer approximation of the microstructure of real polycrystalline materials compared to classical Voronoi tessellation [1, 36–38].

To estimate the size of the reconstructed space, it was assumed that it should ensure a number of tessellation cells (representing 3D grains) comparable to the number of particles indexed on the source SEM images. Therefore, the parameter N_A, which, assuming the sphericity of the cells, is related to N_V by the relationship [39]:

$$N_V = \frac{\sqrt{6\pi}}{6} N_A^{3/2} \tag{3}$$

Since the expected size of the reconstructed space was large, in order to speed up the generation of the synthetic structures it was assumed that a multiple realization of smaller dimensions would be performed, which together would constitute a statistically equivalent volume element (SVE) [1, 22]. To optimize the tessellation structures, in addition to the distribution of equivalent grain diameters (3D), the distribution of the solidity shape descriptor f_s was also utilized. The entire process related to generating tessellation structures was conducted using the Neper program (GNU General Public License) [40, 41].

3. RESULTS

3.1. Quantitative microstructure analysis

The results of the quantitative analysis of the microstructure of the studied polycrystalline zirconia were obtained based on 50 SEM images taken at a magnification of 50000×. The directly determined and calculated values of selected microstructural parameters are presented in Table 1.

Table 1
Values of some quantitative microstructure parameters: N_{tot} – total number of counted particles, A_{tot} – total area of counted particles, $\langle A\rangle$ – average particle area, N_A – number of particles per unit area, $\langle L\rangle$ – average particle perimeter, $\langle F_{\max}\rangle$ and $\langle F_{\min}\rangle$ – average value of the maximum and minimum Feret diameter, $\langle d_{\mathrm{eq}}\rangle$ – average equivalent diameter, $\langle f_c\rangle$ – average value of the circularity shape descriptor, $\langle f_s\rangle$ – average value of the solidity shape descriptor

N_{tot}	A_{tot}	$\langle A\rangle$	N_A	$\langle L\rangle$	$\langle F_{\max}\rangle$	$\langle F_{\min}\rangle$	$\langle d_{\mathrm{eq}}\rangle$	$\langle f_c\rangle$	$\langle f_s\rangle$
–	μm^2	μm^2	μm^{-2}	μm	μm	μm	μm	–	–
8227	1043	0.127	7.89	1.36	0.470	0.335	0.402	0.726	0.915

To illustrate the variability of some of the determined microstructural parameters, the data collected for them are presented in the form of histograms in Figure 2. The distribution of equivalent diameter values D_{eq}, obtained based on the transformation using the SSS method, is also presented in histogram form (Fig. 2d).

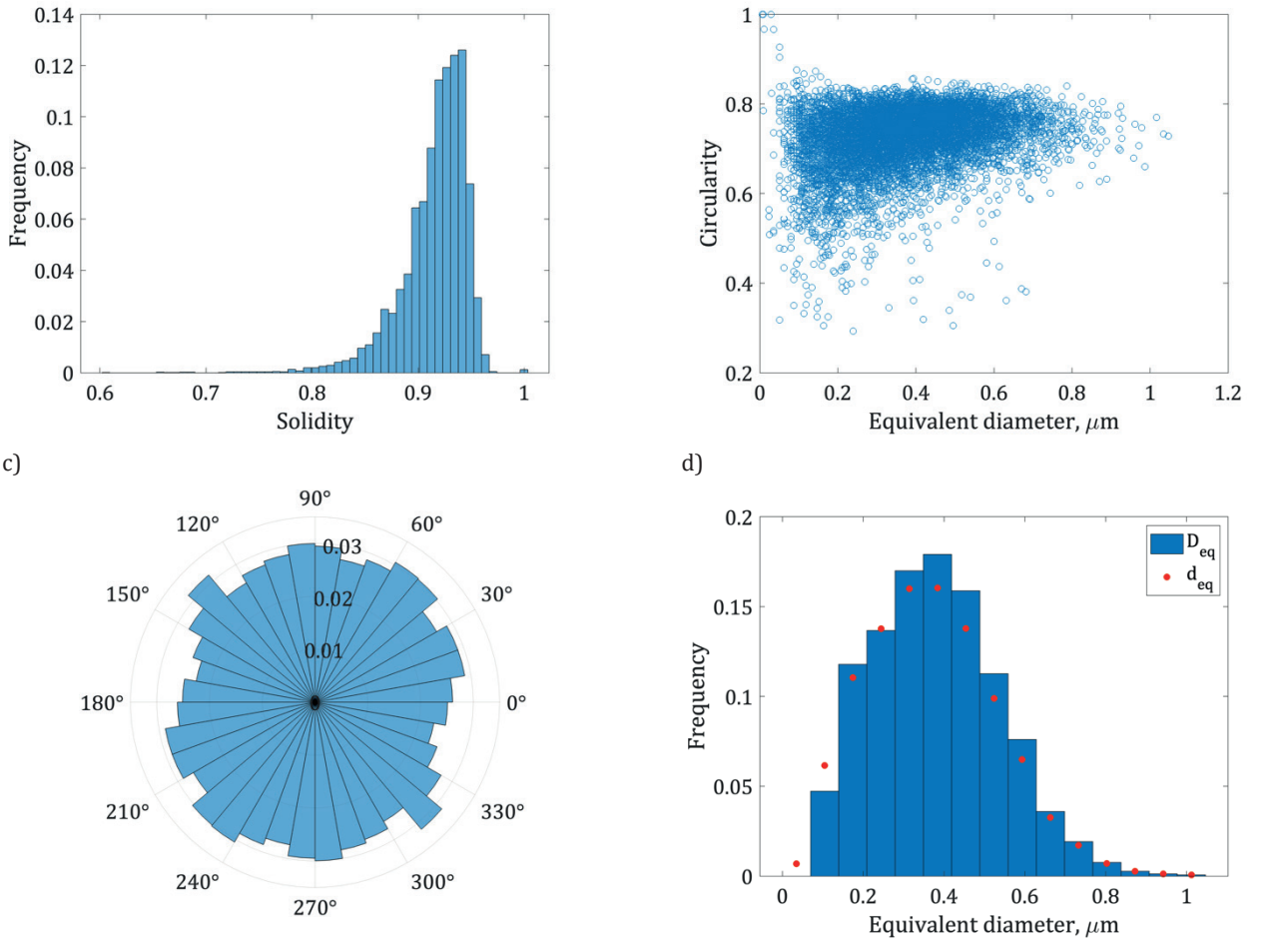

Fig. 2. Some microstructure parameters: (a) histogram of values solidity shape descriptor f_s; (b) relationship between the shape factor f_c and the equivalent diameter of the particles d_{eq}; (c) distribution of angles θ_{max} for the maximum Feret diameters (direction rose); (d) histogram of equivalent grain diameters D_{eq} (3D, represented by blue bars) with highlighted frequency values for equivalent diameters of particles d_{eq} (2D, shown as red dots)

3.2. Microstructure reconstruction

Based on the total number of indexed particles in the SEM images N_{tot} = 8227, the determined parameter N_A = 7.89 μm^{-2}, and the calculated N_V = 16 μm^{-3} from Equation (3), the total volume of the reconstructed space V_{tot} = 514 μm^3 was established, corresponding to a cube with a side length of a = 8 μm. However, for computation optimization, subsequent realizations comprising the SVE had V_i = 27 μm^3 (a = 3 μm). To achieve the SVE, 19 realizations were planned, but the anticipated number of grains was reached after only 15 realizations. An example synthetic microstructure obtained through tessellation is presented in Figure 3a, and a random cross-section of the structure is shown in Figure 3b.

For the geometric models obtained through tessellation, basic microstructure parameters were determined and compiled in Table 2. To illustrate the variability of the equivalent diameters and the variability of the shape descriptor, the collected data are presented as histograms in Figure 3.

Table 2
Values of some quantitative microstructure parameters for the tessellation model: N_{tot} – total number of counted cells, V_{tot} – total volume of counted cells, $\langle V \rangle$ – average cell volume, N_V – number of cells per unit volume, $\langle D_{eq} \rangle$ – average equivalent diameter of the cell

N_{tot}	V_{tot}	$\langle V \rangle$	N_V	$\langle D_{eq} \rangle$
–	μm^3	μm^3	μm^{-3}	μm
9345	405	0.0433	23.1	0.385

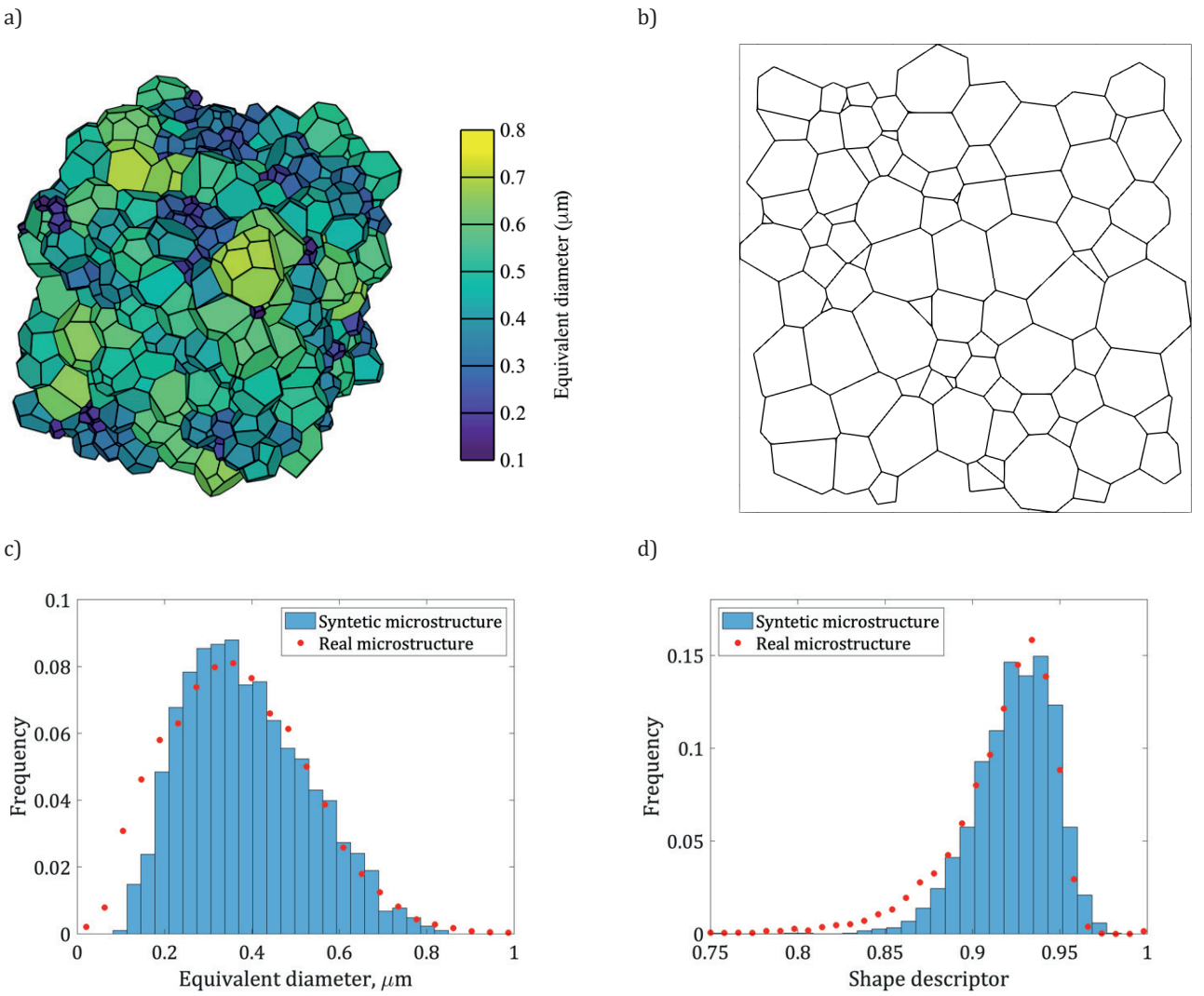

Fig. 3. The results of the microstructure reconstruction conducted using the Laguerre tessellation method: (a) an example synthetic microstructure (the color scale corresponds to the grain size D_{eq}; (b) a cross-section of the synthetic microstructure; (c) distributions of equivalent diameters: determined based on SEM images (red dots) and determined for the synthetic microstructure (blue bars); (d) distributions of shape descriptors: determined based on SEM images (red dots) and determined for the synthetic microstructure (blue bars)

3.3. Results discussion

Based on the qualitative analysis of the SEM images, it can be concluded that the studied TZP possesses a typical microstructure for tetragonal zirconia polycrystalline. The images are dominated by isometric, convex particles whose size does not exceed 1 μm. These observations are confirmed by the results of the quantitative image analysis. The distribution of equivalent particle diameters d_{eq} (2D) and the distribution of equivalent grain diameters D_{eq} (3D) obtained by the SSS method indicate (Fig. 2d) that the material consists of submicron grains, with an average diameter of approximately 0.4 μm. Both the particle size distribution and the grain size distribution are right-skewed, which is well motivated by the theory of sintering ceramic materials. The isometric shape of the particles is confirmed by the distribution of the solidity shape descriptor f_s (Fig. 2a). This distribution is narrow, and $\langle f_s \rangle$ = 0.915 (Tab. 1). It is noteworthy that larger particles are usually more isometric than smaller ones. This is illustrated by the relationship between the circularity shape descriptor f_c and the equivalent diameter d_{eq} presented in Figure 2b. Additionally, the analysis of the distribution of angles θ_{max} for the maximum Feret diameters (Fig. 2c) indicates that the polycrystal obtained through free sintering does not exhibit significant anisotropy in the arrangement of particles.

The presence of isometric, convex particles in SEM images validates the rationale for using the SSS method to transform the distribution of particle diameters d_{eq} into the distribution of grain diameters D_{eq}. Transitioning between dimensions is essential for obtaining the necessary data to reconstruct the microstructure in three dimensions.

Understanding the variability of D_{eq} allowed for the determination of weight coefficients w_i in Laguerre tessellation, thereby generating a synthetic microstructure of TZP (Fig. 3a). The distribution of the size of tessellation cells (virtual grains) in the geometric models shows good agreement with the assumed distribution of equivalent grain

diameters (Fig. 3c). A slight deviation is only observed in the population of the smallest grains. Also, the comparison of N_V values calculated based on the Equation (3), which is based on the assumption of sphericity of monodisperse cells, indicates that the number of tessellation cells in the generated microstructure is higher. The deviation likely results from the asymmetric distribution of equivalent diameter sizes.

Observing the cross-sections of the tessellation structure (Fig. 3b), one can notice a significant similarity in the morphology of tessellation cells compared to the morphology of particles visible in the SEM images. The shape of the cells, especially the largest ones, is isometric, which is consistent with observations and results of the microstructure analysis of the real material. Since the distribution of the shape descriptor was additionally used during the optimization of tessellation structures, the obtained variability in shape is close to the expected (Fig. 3d). However, here too, there is a slight deviation, mainly in the range of the smallest shape descriptor values.

4. CONCLUSIONS

Summarizing the obtained results, it can be stated that:

1. The structure obtained through Laguerre tessellation is a good geometric model of tetragonal zirconia polycrystalline. The most important microstructure parameters, such as the distribution of grain sizes and their shape, are consistent with the assumed values in the model.
2. To achieve a statistically equivalent, synthetic microstructure of tetragonal zirconia polycrystalline, one can use data obtained based on standard stereological measurements, conducted solely on SEM images.
3. The reconstruction pathway presented in the study enables the generation of three-dimensional geometric models that can be used as the basis for a wide range of microstructural analyses. After complementing the tessellation geometric model with material data, it can form the basis for numerical analyses conducted by the finite element method.

Acknowledgements

Particular thanks are owed to Dr Agnieszka Wojteczko of the Faculty Laboratory of Scanning Microscopy and Microanalysis at WIMiC, AGH University of Krakow for taking the SEM images of the microstructure of the material studied in this work. I would also like to thank Prof. Zbigniew Pędzich of WIMiC AGH for providing the TZP samples.

This work was supported by the subvention of the Polish State Ministry of Education and Science for AGH University of Krakow under project 16.16.160.557.

REFERENCES

[1] Grabowski G. (2022). *Mikrostruktura jako podstawa modelowania numerycznego właściwości tworzyw ceramicznych*. Kraków: Wydawnictwo Naukowe „Akapit".

[2] Salvo L., Suéry M., Marmottant A., Limodin N. & Bernard D. (2010). 3D imaging in material science: Application of X-ray tomography. *Comptes Rendus Physique*, 11(9–10), 641–649. DOI: https://doi.org/10.1016/j.crhy.2010.12.003.

[3] Reischig P., King A., Nervo L., Viganó N., Guilhem Y., Palenstijn W.J., Batenburg K.J., Preuss M. & Ludwig W. (2013). Advances in X-ray diffraction contrast tomography: flexibility in the setup geometry and application to multiphase materials. *Journal of Applied Crystallography*, 46(2), 297–311. DOI: https://doi.org/10.1107/S0021889813002604.

[4] Maire E. & Withers P.J. (2014). Quantitative X-ray tomography. *International Materials Reviews*, 59(1), 1–43. DOI: https://doi.org/10.1179/1743280413Y.0000000023.

[5] Poulsen H. (2020). Multi scale hard X-ray microscopy. *Current Opinion in Solid State and Materials Science*, 24(2), 100820. DOI: https://doi.org/10.1016/j.cossms.2020.100820.

[6] Faryna M., Głowiński K., Chulist R. & Pędzich Z. (2023). Influence of sintering conditions on anisotropy of grain boundary networks and microstructure topology in yttria-stabilized zirconia. *Metallurgical and Materials Transactions A: Physical Metallurgy and Materials Science*, 54(11), 4372–4386. DOI: https://doi.org/10.1007/s11661-023-07171-0.

[7] Groeber M.A., Haley B.K., Uchic M.D., Dimiduk D.M. & Ghosh S. (2006). 3D reconstruction and characterization of polycrystalline microstructures using a FIB–SEM system. *Materials Characterization*, 57(4–5), 259–273. DOI: https://doi.org/10.1016/j.matchar.2006.01.019.

[8] Uchic M.D., Holzer L., Inkson B.J., Principe E.L. & Munroe P. (2007). Three-dimensional microstructural characterization using focused ion beam tomography. *MRS Bulletin*, 32(5), 408–416. DOI: https://doi.org/10.1557/mrs2007.64.

[9] Bobrowski P., Pędzich Z. & Faryna M. (2015). Three-dimensional microstructural characterization of porous cubic zirconia. *Micron*, 78, 73–78. DOI: https://doi.org/10.1016/j.micron.2015.07.004.

[10] Bobrowski P., Faryna M. & Pędzich Z. (2017). Microstructural characterization of yttria-stabilized zirconia sintered at different temperatures using 3D-EBSD, 2D-EBSD and stereological calculations. *Journal of Materials Engineering and Performance*, 26(10), 4681–4688. DOI: https://doi.org/10.1007/s11665-017-2794-4.

[11] Schlüter S., Sheppard A., Brown K. & Wildenschild D. (2014). Image processing of multiphase images obtained via X-ray microtomography: A review. *Water Resources Research*, 50(4), 3615–3639. DOI: https://doi.org/10.1002/2014WR015256.

[12] Madej L. (2017). Digital/virtual microstructures in application to metals engineering – A review. *Archives of Civil and Mechanical Engineering*, 17(4), 839–854. DOI: https://doi.org/10.1016/j.acme.2017.03.002.

[13] Bargmann S., Klusemann B., Markmann J., Schnabel J.E., Schneider K., Soyarslan C. & Wilmers J. (2018). Generation of 3D representative volume elements for heterogeneous materials: A review. *Progress in Materials Science*, 96, 322–384. DOI: https://doi.org/10.1016/j.pmatsci.2018.02.003.

[14] Bostanabad R., Zhang Y., Li X., Kearney T., Brinson L.C., Apley D.W., Liu W.K. & Chen W. (2018). Computational microstructure characterization and reconstruction: Review of the state-of-the-art techniques. *Progress in Materials Science*, 95, 1–41. DOI: https://doi.org/10.1016/j.pmatsci.2018.01.005.

[15] Kumar S., Kurtz S.K., Banavar J.R. & Sharma M.G. (1992). Properties of a three-dimensional Poisson–Voronoi tesselation: A Monte Carlo study. *Journal of Statistical Physics*, 67(3–4), 523–551. DOI: https://doi.org/10.1007/BF01049719.

[16] Frazier W.E., Hu S. & Joshi V.V. (2020). A Potts Model parameter study of particle size, Monte Carlo temperature, and "Particle-Assisted Abnormal Grain Growth". *Computational Materials Science*, 185, 109945. DOI: https://doi.org/10.1016/j.commatsci.2020.109945.

[17] Madej L., Sieradzki L., Sitko M., Perzynski K., Radwanski K. & Kuziak R. (2013). Multi scale cellular automata and finite element based model for cold deformation and annealing of a ferritic-pearlitic microstructure. *Computational Materials Science*, 77, 172–181. DOI: https://doi.org/10.1016/j.commatsci.2013.04.020.

[18] Svyetlichnyy D.S. (2014). A three-dimensional frontal cellular automaton model for simulation of microstructure evolution-initial microstructure module. *Modelling and Simulation in Materials Science and Engineering*, 22(8), 085001. DOI: https://doi.org/10.1088/0965-0393/22/8/085001.

[19] Ogawa J. & Natsume Y. (2021). Three-dimensional large-scale grain growth simulation using a cellular automaton model. *Computational Materials Science*, 199, 110729. DOI: https://doi.org/10.1016/j.commatsci.2021.110729.

[20] Ghosh S., Lee K. & Moorthy S. (1995). Multiple scale analysis of heterogeneous elastic structures using homogenization theory and Voronoi cell finite element method. *International Journal of Solids and Structures*, 32(1), 27–62. DOI: https://doi.org/10.1016/0020-7683(94)00097-G.

[21] Fritzen F., Böhlke T. & Schnack E. (2009). Periodic three-dimensional mesh generation for crystalline aggregates based on Voronoi tessellations. *Computational Mechanics*, 43(5), 701–713. DOI: https://doi.org/10.1007/s00466-008-0339-2.

[22] Grabowski G. (2019). Modelling of thermal expansion of single- and two-phase ceramic polycrystals utilizing synthetic 3D microstructures. *Computational Materials Science*, 156, 7–16. DOI: https://doi.org/10.1016/j.commatsci.2018.09.020.

[23] Carneiro P.M., Gamboa P.V., Baudín C. & Silva A.P. (2020). Modelling of elastic modulus of a biphasic ceramic microstructure using 3D representative volume elements. *Journal of the European Ceramic Society*, 40(3), 901–910. DOI: https://doi.org/10.1016/j.jeurceramsoc.2019.10.046.

[24] Grabowski G. (2017). Trójwymiarowa rekonstrukcja mikrostruktury polikrystalicznego tlenku glinu metodą teselacji Laguerre'a. *Materiały Ceramiczne/ Ceramic Materials*, 69(3), 252–257.

[25] Telley H., Libeling T.M. & Mocellin A. (1996). The Laguerre model of grain growth in two dimensions II. Examples of coarsening simulations. *Philosophical Magazine Part B*, 73(3), 409–427. DOI: https://doi.org/10.1080/13642819608239126.

[26] Johansson S.A., Öhman M., Ekh M. & Wahnström G. (2019). CCBuilder: a software that produces synthetic microstructures of WC-Co cemented carbides. *International Journal of Refractory Metals and Hard Materials*, 78, 210–218. DOI: https://doi.org/10.1016/j.ijrmhm.2018.09.011.

[27] Quey R. & Kasemer M. (2022). The Neper/FEPX Project: Free / Open-source Polycrystal Generation, Deformation Simulation, and Post-processing. *IOP Conference Series: Materials Science and Engineering* 1249(1). DOI: https://doi.org/10.1088/1757-899X/1249/1/012021.

[28] Castle M. & Keller J. (2023). Rolling Ball Background Subtraction. https://imagej.net/ij/plugins/rolling-ball.html [accessed: 12.02.2025].

[29] Leymarie F. & Levine M. (1992). Fast raster scan distance propagation on the discrete rectangular lattice. *CVGIP: Image Understanding*, 55(1), 84–94. DOI: https://doi.org/10.1016/1049-9660(92)90008-Q.

[30] Legland D., Arganda-Carreras I. & Andrey P. (2016). MorphoLibJ: integrated library and plugins for mathematical morphology with ImageJ. *Bioinformatics*, 32(22), 3532–3534. DOI: https://doi.org/10.1093/bioinformatics/btw413.

[31] Rasband W.S. (2020). ImageJ. https://imagej.net/ij/ [accessed: 12.02.2025].

[32] Scheil E. (1931). Die Berechnung der Anzahl und Größenverteilung kugelförmiger Kristalle in undurchsichtigen Körpern mit Hilfe der durch einen ebenen Schnitt erhaltenen Schnittkreise. *Zeitschrift für Anorganische und Allgemeine Chemie*, 201(1), 259–264. DOI: https://doi.org/10.1002/zaac.19312010123.

[33] Schwartz H.A. (1934). The metallographic determination of the size distribution of temper carbon nodules. *Metals and Alloys*, 5, 139–140.

[34] Салтыков С.А. (1958). Стереометрическая металлография. Изд. 2-е. Москва: Металлургиздат [Saltykov S.A. (1958). Stereometric Metallography. 2nd Edition. Moscow: Metallurgizdat].

[35] Takahashi J. & Suito H. (2003). Evaluation of the accuracy of the three-dimensional size distribution estimated from the Schwartz–Saltykov method. *Metallurgical and Materials Transaction A*, 34(1), 171–181. DOI: https://doi.org/10.1007/s11661-003-0218-6.

[36] Fan Z., Wu Y., Zhao X. & Lu Y. (2004). Simulation of polycrystalline structure with Voronoi diagram in Laguerre geometry based on random closed packing of spheres. *Computational Materials Science*, 29(3), 301–308. DOI: https://doi.org/10.1016/j.commatsci.2003.10.006.

[37] Wu Y., Zhou W., Wang B. & Yang F. (2010). Modeling and characterization of two-phase composites by Voronoi diagram in the Laguerre geometry based on random close packing of spheres. *Computational Materials Science*, 47(4), 951–961. DOI: https://doi.org/10.1016/j.commatsci.2009.11.028.

[38] Liebscher A., Jeulin D. & Lantuéjoul C. (2015). Stereological reconstruction of polycrystalline materials. *Journal of Microscopy*, 258(3), 190–199. DOI: https://doi.org/10.1111/jmi.12232.

[39] de Souza D.S., da Silva Assis W.L., Rios P.R. & da Fonseca G.S. (2014). Stereological analysis of the microstructure of pure iron with random nucleation. *Journal of Materials Research and Technology*, 3(4), 349–353. DOI: https://doi.org/10.1016/j.jmrt.2014.08.002.

[40] Quey R. (2023). Neper. https://neper.info/ [accessed: 12.02.2025].

[41] Quey R., Dawson P. & Barbe F. (2011). Large-scale 3D random polycrystals for the finite element method: Generation, meshing and remeshing. *Computer Methods in Applied Mechanics and Engineering*, 200(17–20), 1729–1745. DOI: https://doi.org/10.1016/j.cma.2011.01.002.